Jing and Guo *Chin. J. Mech. Eng.* (2019) 32:63
https://doi.org/10.1186/s10033-019-0378-y

Chinese Journal of Mechanical Engineering

ORIGINAL ARTICLE Open Access

Modeling and Configuration Design of Electromagnetic Actuation Coil for a Magnetically Controlled Microrobot

Xiaolong Jing and Weizhong Guo*

Abstract

Non-contact actuated microbeads have attracted a lot of attention in recent years because of its enormous potential in medical, biological, and industrial applications. Researchers have proposed a multitude of electromagnetic actuation (EMA) systems consisting of a variety of coil pairs. However, a unified method to design and optimize a coil pair according to technical specifications still does not exist. Initially, this paper presented the modeling of an untethered ferromagnetic particle actuated by externally applied magnetic field. Based on the models, a simple method of designing and optimizing the EMA coil pair according to technical specifications, was proposed. A loop-shaped coil pair generating uniform magnetic and gradient fields was chosen to demonstrate this method clearly and practically. The results of the optimization showed that the best distance to radius ratio of a loop-shaped coil pair is 1.02 for a uniform magnetic field and 1.75 for a uniform gradient field. The applicability of the method to other shapes of coil configuration was also illustrated. The best width to distance ratio for a square-shaped coil pair is 0.558 and 0.958 for uniform magnetic and gradient fields, respectively. The best height to width ratio and distance to width ratio for a rectangle-shaped coil pair is $h/w = [0.9,1.1]$, $d/w = [0.5,0.6]$ for uniform magnetic field and $h/w = [1.0,1.2]$, $d/w = [0.9,1.1]$ for uniform gradient field. Furthermore, simulations of a microparticle tracking the targeted trajectory were conducted to analyze the performance of the newly designed coils. The simulations suggested the ability of manipulating microparticles via the coils designed by our proposed method. The research mainly proposed a unified design and optimization method for a coil pair, which can support researchers while designing a specific coil pair according to the technical requirements. This study is aimed at researchers who are interested in EMA system and microrobots.

Keywords: Micro-robot/particle, Coil configuration design and optimization, Electromagnetic actuation, Trajectory tracking

1 Introduction

Microrobots hold great promise for a large amount of applications, including minimally invasive surgery, targeted drug delivery, and micromanipulation [1–3]. However, as the size of the microrobots decreases, traditional mechanical structures, based on the use of links and joints, suffer from lack of direct contact during the delivering of motion and energy supply. One feasible solution is electromagnetic actuation (EMA), specifically, magnetic microrobots. Magnetic microrobots [4–6] are simple devices actuated by an externally applied magnetic field, which exerts combinations of magnetic forces and torques upon the microrobots without any direct contact. Three main driving fields have been proposed: alternating field, rotating field, and gradient field.

An alternating field is a field whose amplitude and direction vary over time according to certain rules. Two main alternating-field-based actuation mechanisms have been proposed in recent years: oscillating-uniform-field-based and pulsed-field-based actuation. An oscillating uniform field can oscillate or rotate within a certain angle, which produces thrust force to propel the

*Correspondence: wzguo@sjtu.edu.cn
Institute of Design and Control Engineering for Heavy Equipment, School of Mechanical Engineering, Shanghai Jiao Tong University, Shanghai 200240, China

microrobot to swim forward similar to the tail fin of a fish [7–9]. A pulsed magnetic field can induce stick-slip behaviors in the micro-robot [10, 11], causing it to translate on arbitrary surfaces.

A rotating field is a field that has moving polarities in which its opposite poles rotate around a central axis, which drives the microrobot to rotate together with the field and produces propulsive motion like the helical-shaped bacteria. The rotating-field-based actuation can be grouped into three main mechanisms: rolling, propelling, and swimming [12]. This method of actuation is favored by numerous researchers because of its simplicity. The fabrication, control, and application of an artificial bacterial flagella actuated by a rotating magnetic field was introduced in [13–15] and optimization of the robot shape and rotating field frequency were discussed in [14, 16].

Generally, owing to the manufacturing difficulties, poor turning performance, and low motion speed of the microrobots actuated by alternating or rotating fields, the gradient field is a preferable alternative. The gradient field can exert magnetic forces and torques on any ferromagnetic particle. A host of gradient-field-based driving mechanisms were reported in the past several years. Different configurations of gradient-field-based EMA systems [17–22] were proposed for various purposes. Further, to improve controllability and mane maneuverability of the microrobots, a variety of novel methods were also proposed. An enhanced EMA system was proposed to enable the effective manipulation of microparticles in a considerably larger workspace with higher effectiveness [23–25]. A steering system with coaxial Maxwell and Helmholtz coil pairs rotating around the workspace to control the orientation and direction of magnetic thrust vector was proposed to achieve an in-plane three-degrees-of-freedom motion with the minimum number of coils [26]. An EMA system consisting of a pair each of stationary and rotational Helmholtz–Maxwell coils can manipulate a microrobot in 3-dimensional space and in the phantom of a blood vessel [27]. A novel system that was composed of one conventional pair of Maxwell and Helmholtz coils and one newly developed pair of gradient and uniform saddle coils demonstrated a more geometrically compact and magnetically efficient system than the conventional systems [28, 29]. In addition, special applications of magnetic robots were also developed. A system called OctoMag was designed to control intraocular microrobots for delicate retinal procedures [30]. A novel method of controllable disassembly of paramagnetic nanoparticle chains, using a predefined dynamic field generated by a three-axis Helmholtz electromagnetic coils system, was proposed for microrobotic cargo delivery [31].

However, even though various gradient-field-based systems and methods have been proposed, a unified method to design and optimize a specific gradient-field-based coil pair configuration according to technical requirements is yet to be developed. This paper presented the modeling of the behaviors of an object actuated by a gradient field, including the current, magnetics, and dynamic behaviors. Furthermore, based on the models, a general and simple method was proposed for EMA coil configuration design and optimization according to certain technical specifications. In addition, the design of uniform magnetic and gradient fields with a loop-shaped coil, acting as the basic shape of the coil, is used to illustrate the designing and optimizing process. Applicability of the optimization method to other kinds of coil configuration is also illustrated. Finally, through simulations, the validity of the models and the simple method was evaluated.

This paper is organized as follows: Section 2 presents the modeling equations of microrobot controlled by a gradient field. Section 3 discusses the EMA coil configuration design and optimization method and an example is used to demonstrate it clearly. Applicability of the method to other coil configurations is also discussed in this section. Section 4 provides the simulation results using the optimized coil pair and certain discussions are presented. The conclusion is summarized in Section 5.

2 Modeling of Electromagnetic Actuation

Any ferromagnetic object can be actuated by a gradient-field-based EMA system through three step-by-step processes: (1) The currents flowing in the coils induce nonuniform magnetic field; (2) This externally applied field exerts a combination of forces and torques on the object; (3) The exerted forces and torques propel the object to move. Three models were constructed to describe the three processes, respectively.

2.1 Current Induces Magnetic Field

As is shown in Figure 1, we initially consider the magnetic field distribution induced by a single loop-shaped finite long current-carrying coil. The central axis of the coil is aligned with z-axis of the cylindrical coordinate. The length and radius of the coil are l and a, respectively. The magnitude of current flowing in the coil is I, with number of turns N.

The magnetic field [32, 33] at the position of (ρ, z) can be expressed as follows:

$$B_\rho = \frac{\mu_0 NI}{4\pi}\sqrt{\frac{a}{\rho}}\left[\frac{k-2}{\sqrt{k}}\boldsymbol{K}\left(\sqrt{k}\right)+\frac{2}{\sqrt{k}}\boldsymbol{E}\left(\sqrt{k}\right)\right]_{k-}^{k+}, \tag{1}$$

$$B_z = -\frac{\mu_0 NI}{4\pi}\frac{1}{\sqrt{a\rho}}\left[\xi\sqrt{k}\boldsymbol{K}\left(\sqrt{k}\right)+\xi\sqrt{k}\prod\left(h,\sqrt{k}\right)\right]_{k-}^{k+}, \tag{2}$$

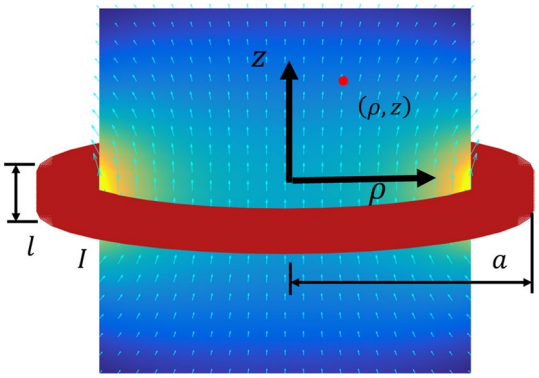

Figure 1 Finite long current-carrying loop-shaped coil

where

$$\xi\pm = z \pm \frac{l}{2}, \tag{3}$$

$$k\pm = \frac{4a\rho}{(a+\rho)^2+\xi^2}, \tag{4}$$

$$h = \frac{4a\rho}{(a+\rho)^2}. \tag{5}$$

However, because of the elliptic integrals, $\boldsymbol{E}$, $\boldsymbol{K}$, $\boldsymbol{\Pi}$, fast calculation of the magnetic field is difficult. Besides, using these formulae to design a magnetic field quantitatively is an impossible task. Therefore, optimization of the equations was required. According to Ref. [34], elliptic integrals can be expanded as a sum of infinite series. We used the first few items of the elliptic integral expansions to approximate the accurate value, thus, the elliptic integrals can be approximated by:

$$\boldsymbol{E}(k) = \frac{\pi}{2}\left[1 - \frac{1}{4}k^2\right], \tag{6}$$

$$\boldsymbol{K}(k) = \frac{\pi}{2}\left[1 + \frac{1}{4}k^2\right], \tag{7}$$

$$\prod(\alpha^2, k) = \frac{\pi}{2\sqrt{1-\alpha^2}} + \frac{\pi^2}{4\alpha^2}\left[\frac{1}{\sqrt{1-\alpha^2}} - 1\right]. \tag{8}$$

The truncation errors were less than 0.2% and were minor enough to be neglected for the calculation of magnetic field. The truncation error of elliptic integrals can occur at any point in space; specifically, it affects the whole scale. Further, in the process of optimizing the coil configuration described in Section 3, normalized values of optimization operators are used for convenience of comparison, which eliminated the whole-scale truncation errors and did not affect the design and optimization result described in Section 3.

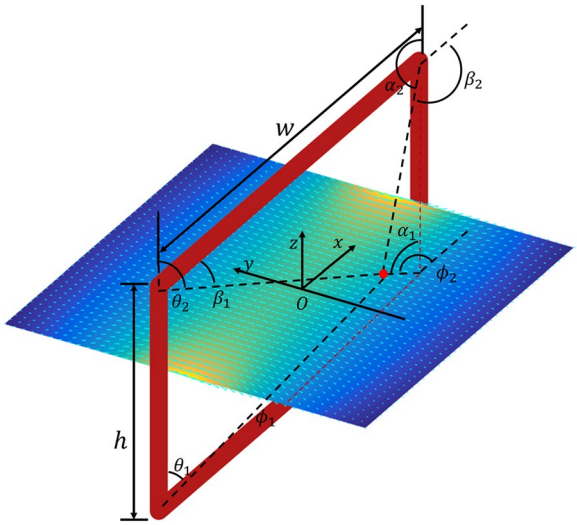

Figure 2 Single current-carrying rectangle-shaped coil

Substituting Eqs. (6)–(8) into Eqs. (1)–(5) yields:

$$B_\rho = \frac{\mu_0 NI}{32l}\sqrt{\frac{a}{\rho}}\left[k^{\frac{3}{2}}\right]_{k-}^{k+}, \tag{9}$$

$$B_z = -\frac{\mu_0 NI}{4l}\frac{1}{\sqrt{a\rho}}\left[\xi\sqrt{k} + \frac{\xi(2a+\rho)k^{\frac{3}{2}}}{8a}\right]_{k-}^{k+}. \tag{10}$$

Quantitative and fast computation of the magnetic field of a loop coil through Eqs. (9)–(10) was realizable. Therefore, it was used to design and optimize an EMA coil pair configuration, which will be introduced in Section 3.

Further, square-shaped or rectangle-shaped coils are also widely used. We present below the magnetic field distribution expressions of these coils for the convenience of optimization. As shown in Figure 2, the field distribution in the *xy*-plane can be expressed as:

$$\begin{aligned} B_x = &-\frac{yi}{(x+w/2)^2+y^2}(\cos\theta_1 - \cos\theta_2) \\ &+ \frac{yi}{(x-w/2)^2+y^2}(\cos\alpha_1 - \cos\alpha_1), \end{aligned} \tag{11}$$

$$
\begin{aligned}
B_y = &+\frac{i(x+w/2)}{(x+w/2)^2+y^2}(\cos\theta_1-\cos\theta_2)\\
&+\frac{-i(z-h/2)}{y^2+(z-h/2)^2}(\cos\beta_1-\cos\beta_2)\\
&+\frac{-i(x-w/2)}{(x-w/2)^2+y^2}(\cos\alpha_1-\cos\alpha_2)\\
&+\frac{i(z+h/2)}{y^2+(z+h/2)^2}(\cos\phi_1-\cos\phi_2),
\end{aligned}
\tag{12}
$$

where

$$
i=\frac{\mu_0 I}{4\pi}. \tag{13}
$$

2.2 Magnetic Field Exerts Forces and Torques on Object

We considered an object created using ferromagnetic material owing to the high susceptibility and magnetization saturation of the material. Any ferromagnetic object in the magnetic field is influenced by the magnetic force and torque induced from the gradient and intensity of the externally applied non-uniform magnetic field [35]. The magnetic force and torque exerted on the object can be expressed by:

$$
\boldsymbol{F}_{mag}=v(\boldsymbol{M}\cdot\nabla)\boldsymbol{B}, \tag{14}
$$

$$
\boldsymbol{T}_{mag}=v\boldsymbol{M}\times\boldsymbol{B}, \tag{15}
$$

where $\boldsymbol{B}$ is the value of intensity—measured in units of Tesla (T)—of the magnetic field at the body's center of mass. $\boldsymbol{B}$ can also be expressed as $\boldsymbol{H}$, which is simply related to $\boldsymbol{B}$ as $\boldsymbol{B}=\mu_0\boldsymbol{H}$, where $\mu_0=4\pi\times10^{-7}\mathrm{T}\cdot\mathrm{m/A}$ is the permeability of free space. $\boldsymbol{M}$ is the magnetization at the body's center of mass. v is the volume of the ferromagnetic object. ∇ is the gradient operator:

$$
\nabla=\left[\frac{\partial}{\partial x},\frac{\partial}{\partial y},\frac{\partial}{\partial z}\right]^{\mathrm{T}}. \tag{16}
$$

Magnetization $\boldsymbol{M}$ can be calculated as:

$$
\boldsymbol{M}=\chi_a\frac{\boldsymbol{B}}{\mu_0}. \tag{17}
$$

χ_a is the equivalent susceptibility of the object expressed as:

$$
\chi_a=\mathrm{diag}\left(\frac{\chi}{1+n_x\chi},\frac{\chi}{1+n_y\chi},\frac{\chi}{1+n_z\chi}\right), \tag{18}
$$

where χ is the susceptibility of the object's material, n_x, n_y, n_z are the demagnetizing factors [36] along (x, y, z)-axes, respectively, of the ellipsoidal object or its magnetically equivalent ellipsoid [37] with semi-minor and semi-major axes aligned with respect to the body frame system's axes.

The components of the magnetization $\boldsymbol{M}$ in (x, y, z)-axes directions can be represented as M_x, M_y, and M_z, respectively. To express the magnetic force and torque in a more intuitive form, Eqs. (14) and (15) can be rewritten, after some manipulation, as:

$$
\begin{bmatrix}F_x\\F_y\\F_z\end{bmatrix}=v\begin{bmatrix}M_x\frac{\partial B_x}{\partial x}+M_y\frac{\partial B_x}{\partial y}+M_z\frac{\partial B_x}{\partial z}\\M_x\frac{\partial B_y}{\partial x}+M_y\frac{\partial B_y}{\partial y}+M_z\frac{\partial B_y}{\partial z}\\M_x\frac{\partial B_z}{\partial x}+M_y\frac{\partial B_z}{\partial y}+M_z\frac{\partial B_z}{\partial z}\end{bmatrix}_{3\times1}, \tag{19}
$$

$$
\begin{bmatrix}T_x\\T_y\\T_z\end{bmatrix}=v\begin{bmatrix}-M_zB_y+M_yB_z\\M_zB_x+M_xB_z\\-M_yB_x+M_xB_y\end{bmatrix}_{3\times1}. \tag{20}
$$

In Eqs. (14)–(20), $\boldsymbol{M}$, $\boldsymbol{H}$, and χ_a are all written with respect to the global coordinate system O-xyz, which has the same orientation as the body frame system $O_1-x_1y_1z_1$, shown in Figure 3(1).

If the body frame system and global system do not have the same orientation, as shown in Figure 3(2), then Eq. (17) can be updated as:

$$
\boldsymbol{M}=\boldsymbol{R}\chi_a\boldsymbol{R}^{\mathrm{T}}\frac{\boldsymbol{B}}{\mu_0}, \tag{21}
$$

where $\boldsymbol{R}$ is the rotation matrix relating the body frame system with respect to the global system, reflecting the impact of the pose of the ellipsoid on the magnetization $\boldsymbol{M}$.

2.3 Forces and Torques Propel the Object to Move

Dynamic behaviors of the object can be modeled by Newton's equation for translational motion and Euler's equation for rotational motion, respectively:

$$
\sum\boldsymbol{F}=m\boldsymbol{g}+\sum\boldsymbol{F}_{mag}+\boldsymbol{F}_{ext}=m\ddot{\boldsymbol{x}}, \tag{22}
$$

$$
\sum\boldsymbol{M}=\sum\boldsymbol{M}_{mag}+\boldsymbol{M}_{ext}=\boldsymbol{I}\dot{\omega}+\omega\times\boldsymbol{I}\omega, \tag{23}
$$

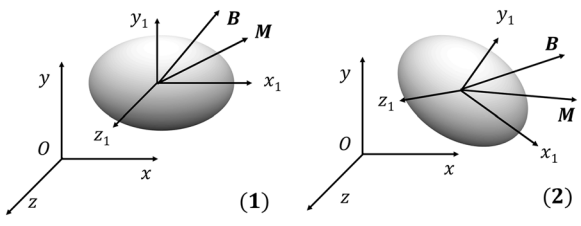

Figure 3 Impact of pose of the axially symmetric ellipsoid

where $\boldsymbol{g}$ is gravitational acceleration, $\sum \boldsymbol{F}_{mag}$, $\sum \boldsymbol{M}_{mag}$ are magnetic forces and torques, respectively, and $\sum \boldsymbol{F}_{ext}$, $\sum \boldsymbol{M}_{ext}$ are external forces and torques, respectively. $\ddot{x}$ is the translational acceleration of the body frame attached to the body's center of mass with respect to the global frame. $\boldsymbol{I}\dot{\omega}$, $\omega \times \boldsymbol{I}\omega$ reflect Coriolis and centrifugal effect, respectively.

3 EMA Coil Configuration Design and Optimization Method

As stated before, although various EMA systems consisting of different types of coil pair configurations were proposed in recent years, no one has reported a universal method to design and optimize a gradient-field-based coil pair. This section will introduce a simple method on this issue. We considered a 2-dimensional EMA system as an example to introduce the method step by step.

3.1 Characteristics of the Field

The first step was to determine the most remarkable and suitable characteristic of the field according to technical specifications.

From Eqs. (19) and (20), it is easy to observe that the magnetic force and torque are functions of position and current. If the magnitude and gradient of the magnetic field in the region of interest were assumed to be constants or pseudo-constants, i.e., $\partial B = 0$ or const, $B = 0$ or const,we could obtain single-valued mappings from currents to magnetic force and torque, which would significantly simplify the design and optimization process. Therefore, the most remarkable characteristic was uniformity of the uniform magnetic and gradient fields. Furthermore, this is also the most common characteristic in most of the gradient-field based EMA systems as is described in Section 1.

3.2 Choosing Appropriate Types of Coil Pairs

The next step was to determine the fundamental shape of the finite long current-carrying coil, which can be a loop-shaped coil [38], a rectangle-shaped coil [39], or even a saddle-shaped coil, and the parameters to be optimized. In this process, certain major factors including compactness of the EMA system, space utilization, and manufacturing difficulties and expenses was taken into consideration.

Generally, it is acknowledged that the conventional loop-shaped Helmholtz coil pair induces uniform magnetic field and the conventional loop-shaped Maxwell coil pair induces uniform gradient field. They are the most commonly used coil pairs in gradient-field-based EMA systems. However, there are no reports to prove that they are the best choices to induce such a field and the reasons for their current coil parameters. To overcome this limitation, we considered a loop-shaped coil pair as an example to illustrate the method to optimize the coil configuration clearly and practically. Section 3.6 will present the applicability of the optimization method on other coil configurations.

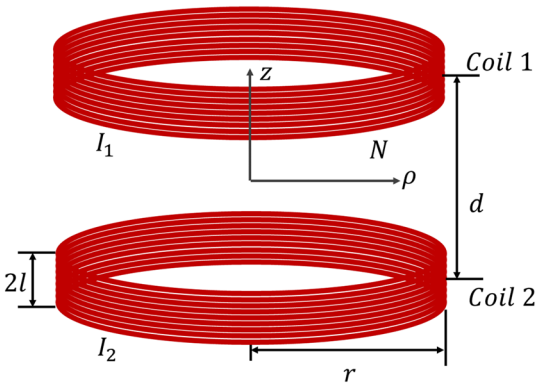

Figure 4 Pair of loop-coils consisting of two single coils with currents of the same magnitude flowing in the coil wires

For a loop-shaped coil pair as shown in Figure 4, r, d, and $2l$ are the distance, radius, and length of the coils, respectively. I_1, I_2 are the magnitude of currents flowing in the coil pair. N is the number of turns of the wire. $2l$ varies with the number of turns N of the current and the size of the wire, which does not have a direct impact on the field distribution. Conversely, I, r, and d have a big impact on the magnetic field distribution, magnitude, and even the type of magnetic field. Therefore, the main optimization task was to optimize them.

3.3 Optimization of the Coil Pair

3.3.1 Optimization Operators

To generalize the optimization process, certain universal optimization operators were defined to meet various requirements of the field. Here, we present a list of these operators:

1) $\partial B = 0$, $B = const$ ensures a uniform field.
2) $\partial B = const$, $B = 0$ ensures a uniform gradient field.
3) $\partial B = 0$, $B = 0$ ensures no magnetic field existing in a specific direction.
4) $\partial^2 B = 0$ ensures absolute uniformity of the uniform magnetic field or the uniform gradient field.
5) $S(args)$ calculates the maximum usable area (MUA) of the magnetic field that conforms to specific uniformity requirements, where *args* are parameters that need to be optimized.
6) $M(args)$ calculates the maximum magnitude of the uniform magnetic field or the maximum gradient of the uniform gradient field, where *args* are parameters that need to be optimized.

3.3.2 Optimization of the Loop-Shaped Coil Pair That Induces Uniform Magnetic Field

If the currents in the two coils flow in the same direction, i.e., $I_1 = I_2 = I$, the coil pair is likely to induce uniform magnetic field along the z-axis in the central area as the field component along the ρ-axis generated by the two coils cancel each other, and thereby remaining the component along the z-axis. The magnetic field of the coil pair is the superposition of the two coils and can be obtained from Eqs. (9) and (10).

The magnetic field along the ρ-axis and its partial derivative with respect to the ρ-axis are expressed as:

$$B_\rho = B_{\rho 1} + B_{\rho 2} = i_\rho \frac{\rho}{r} \sum_{k=1}^{4} \frac{C_k}{\left(n^2 + m_k^2\right)^{\frac{3}{2}}}, \tag{24}$$

$$\frac{\partial B_\rho}{\partial \rho} = \frac{i_\rho}{r} \sum_{k=1}^{4} C_k \frac{\left(n^2 + m_k^2\right) - \frac{3\rho n}{r^2}}{\left(n^2 + m_k^2\right)^{\frac{5}{2}}}, \tag{25}$$

where

$$C_1 = C_3 = 1, C_2 = C_4 = -1, \tag{26}$$

$$n = 1 + \frac{\rho}{r}, \tag{27}$$

$$\begin{aligned} m_1 &= \frac{d}{r}\left(\frac{z}{d} + \frac{1}{2} + \frac{l}{2d}\right), \quad m_2 = \frac{d}{r}\left(\frac{z}{d} + \frac{1}{2} - \frac{l}{2d}\right), \\ m_3 &= \frac{d}{r}\left(\frac{z}{d} - \frac{1}{2} + \frac{l}{2d}\right), \quad m_4 = \frac{d}{r}\left(\frac{z}{d} - \frac{1}{2} - \frac{l}{2d}\right), \end{aligned} \tag{28}$$

$$i_\rho = \frac{\mu_0 NI}{4l}. \tag{29}$$

i_ρ represents a comprehensive influence of parameters that are not required to be optimized, such as currents, number of turns, permeability of free space, and diameter of the wire.

The magnetic field along the z-axis and its partial derivative with respect to the z-axis are expressed as:

$$\begin{aligned} B_z &= B_{z1} + B_{z2} \\ &= i_z \sum_{k=1}^{4} \frac{C_k m_k}{\left(n^2 + m_k^2\right)^{\frac{1}{2}}} \left(1 + \frac{\rho}{r}\left(2 + \frac{\rho}{r}\right) \frac{1}{n^2 + m_k^2}\right), \end{aligned} \tag{30}$$

$$\begin{aligned} \frac{\partial B_z}{\partial z} &= \frac{i_z}{r} \sum_{k=1}^{4} \frac{C_k n^2}{\left(n^2 + m_k^2\right)^{\frac{3}{2}}} \\ &\quad + \frac{i_z \rho}{2r}\left(2 + \frac{\rho}{r}\right) \sum_{k=1}^{4} \frac{C_k \left(n^2 - 2m_k^2\right)}{\left(n^2 + m_k^2\right)^{\frac{5}{2}}}, \end{aligned} \tag{31}$$

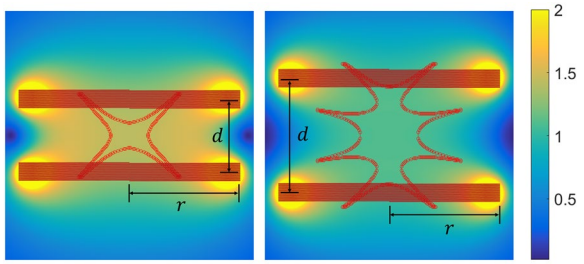

$d/r = 0.7$ $d/r = 1.1$

Figure 5 Magnetic field of the coil pair and its maximum usable region for different d/r

where

$$i_z = -\frac{\mu_0 NI}{2l}. \tag{32}$$

From Eqs. (24)–(32), it is observed that the following optimization operators are naturally satisfied in the central area of the loop-shaped coil pair:

$$B_\rho\big|_{\rho=0,z=0} = 0, \quad \left.\frac{\partial B_\rho}{\rho}\right|_{\rho=0,z=0} = 0, \tag{33}$$

$$B_z|_{\rho=0,z=0} = const, \quad \left.\frac{\partial B_z}{z}\right|_{\rho=0,z=0} = 0. \tag{34}$$

Eq. (33) ensures no magnetic field exists along the ρ-axis. Eq. (34) ensures a uniform field along the z-axis. Therefore, any loop-shaped coil pair with currents flowing in the same direction in each coil induces uniform magnetic field near the central area, the magnitude of which can be expressed in cylindrical coordinate system $O - \rho z$ as:

$$\boldsymbol{B} = \left[0 \quad \frac{-i_z(d+l)}{\sqrt{r^2 + (d+l)^2/4}} + \frac{i_z(d-l)}{\sqrt{r^2 + (d-l)^2/4}}\right]^{\mathrm{T}}. \tag{35}$$

From Eq. (35), it can be observed that the magnitude of the uniform field is a single-valued function of current I in the central area. However, the geometry parameter of the coil pair, i.e., d/r is still unknown. Besides, this parameter has a great impact on the magnitude and MUA of the uniform field. Figure 5 shows the uniform field distribution in the ρz-plane and its MUA for two different values of d/r. The colormap shows the normalized magnitude $B(x, y)/B(0, 0)$ of the field. The region enclosed by the red line represents the MUA, which is defined as the area with perfect uniformity of the field that never deviates from the field at the origin by more than a specific amount of deviation.

The next step was to identify an optimal d/r. Optimization operators $M(d/r)$ and $S(d/r)$ were used. For the

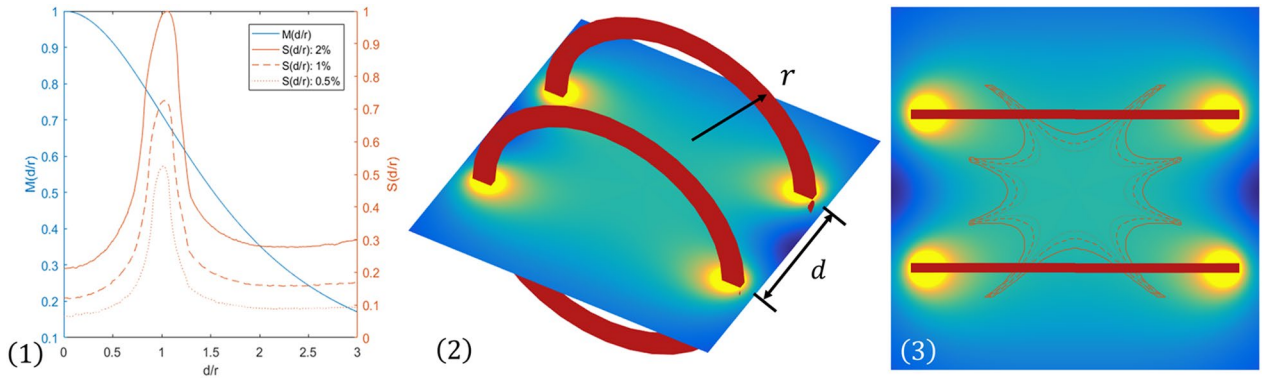

Figure 6 Optimization result for the loop-shaped coil pair inducing uniform magnetic field

convenience of calculation, we defined $S(d/r) = MUA$, $M(d/r) = B_0(d/r)$, where $B_0(d/r)$ is the magnitude of the field at the origin for a specific d/r. The results are shown in Figure 6.

Figure 6(1) shows $M(d/r)$ and $S(d/r)$ of the field. For different uniformity deviations of 2%, 1%, and 0.5%, the $S(d/r)$ reaches the maximum when $d/r = 1.05$, 1.04, and 1.02, respectively. Meanwhile, the magnitude of the field $M(d/r)$ is also large. Figure 6(2) shows the magnetic field distribution for $d/r = 1.02$. Figure 6(3) shows its MUA for different uniformity deviations of 2%, 1%, 0.05%.

Thus, to obtain the best uniform magnetic field, we use of a coil pair with currents flowing in the same direction in each coil and with $d/r = 1.02$ was a perfect choice. In a special case where $d/r = 1.00$, it represents a conventional Helmholtz coil pair. The result proved that the conventional Helmholtz coil pair is one of the best loop-shaped coil pairs to induce uniform magnetic field.

3.3.3 Optimization of the Loop-Shaped Coil Pair That Induces Uniform Gradient Field

Similarly, if the currents flow in opposite directions in each coil, i.e., $I_1 = -I_2 = I$, the coil pair is likely to induce uniform gradient field as the magnitude of the field generated by the two coils cancel each other in the central area. The field distribution and its partial derivative can be similarly obtained from Eqs. (9) and (10) expressed as follows:

$$B_\rho = B_{\rho 1} + B_{\rho 2} = i_\rho \frac{\rho}{r} \sum_{k=1}^{4} \frac{D_k}{\left(n^2 + m_k^2\right)^{\frac{3}{2}}}, \tag{36}$$

$$\frac{\partial B_\rho}{\partial \rho} = \frac{i_\rho}{r} \sum_{k=1}^{4} D_k \frac{\left(n^2 + m_k^2\right) - \frac{3\rho n}{r^2}}{\left(n^2 + m_k^2\right)^{\frac{5}{2}}}, \tag{37}$$

$$\begin{aligned} B_z &= B_{z1} + B_{z2} \\ &= i_z \sum_{k=1}^{4} \frac{D_k m_k}{\left(n^2 + m_k^2\right)^{\frac{1}{2}}} \left(1 + \frac{\rho}{r}\left(2 + \frac{\rho}{r}\right) \frac{1}{n^2 + m_k^2}\right), \end{aligned} \tag{38}$$

$$\begin{aligned} \frac{\partial B_z}{\partial z} &= \frac{i_z}{r} \sum_{k=1}^{4} \frac{D_k n^2}{\left(n^2 + m_k^2\right)^{\frac{3}{2}}} \\ &\quad + \frac{i_z \rho}{2r}\left(2 + \frac{\rho}{r}\right) \sum_{k=1}^{4} \frac{D_k \left(n^2 - 2m_k^2\right)}{\left(n^2 + m_k^2\right)^{\frac{5}{2}}}, \end{aligned} \tag{39}$$

where

$$D_1 = D_4 = 1, \quad D_2 = D_3 = -1. \tag{40}$$

From Eqs. (36)–(40), we observed that in the central area of the loop-shaped coil pair the following operators were naturally satisfied:

$$B_\rho\big|_{\rho=0,z=0} = 0, \quad \left.\frac{\partial B_\rho}{\rho}\right|_{\rho=0,z=0} = const, \tag{41}$$

$$B_z|_{\rho=0,z=0} = 0, \quad \left.\frac{\partial B_z}{z}\right|_{\rho=0,z=0} = 2const. \tag{42}$$

Eqs. (41) and (42) ensure uniform gradient field both along the ρ- and z-axis. Therefore, any loop-shaped coil pair with currents flowing in opposite directions in each coil induces uniform gradient field near the central area, the gradient magnitude of which can be expressed in cylindrical coordinate system $O - \rho z$ as follows:

$$\partial \boldsymbol{B} = \left[\, du \;\; 2du \,\right]^{\mathrm{T}}, \tag{43}$$

where

$$du = \frac{\frac{1}{2}\frac{-\mu_0 NI}{l}r^2}{\left(r^2+(d+l)^2/4\right)^{\frac{3}{2}}} + \frac{\frac{1}{2}\frac{\mu_0 NI}{l}r^2}{\left(r^2+(d+l)^2/4\right)^{\frac{3}{2}}}. \tag{44}$$

From Eqs. (43) and (44), it can be observed that the magnitude of the uniform gradient field is a single-valued function of current I in the central area. Besides, d/r also has a great impact on the amplitude and MUA of the gradient field. Figure 7 shows the gradient field distribution and its gradient along the z-axis in the ρz-plane.

Figure 7(1) shows the magnetic field distribution of the uniform gradient field. Figure 7(2) shows its gradient along the *z-axis*. The region enclosed by red circles in Figure 7(3) and 7(4) represent the MUA for $d/r = 1.1$ and 1.6, respectively.

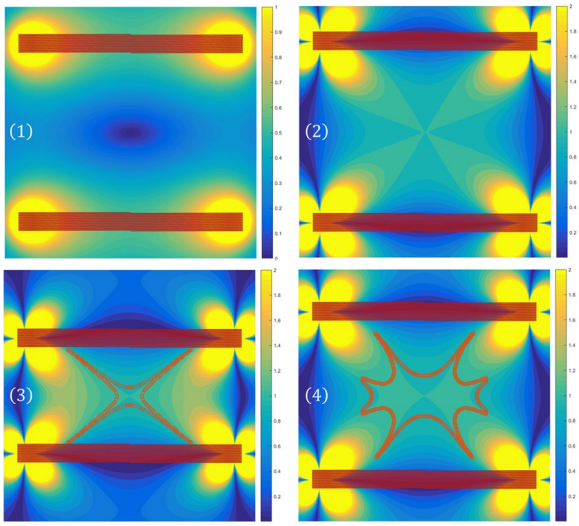

Figure 7 Uniform gradient field distribution and its gradient along z-axis of the coil pair

We defined $S(d/r) = MUA$, $M(d/r) = \partial B_{z0}(d/r)$, where $B_{z0}(d/r)$ is the magnitude of the gradient at the origin along the *z-axis* for a specific d/r. The results are shown in Figure 8.

Figure 8(1) shows $M(d/r)$ and $S(d/r)$ of the field. For different uniformity deviations of 2%, 1%, and 0.5%, the $S(d/r)$ reaches the maximum when $d/r = 1.78$, 1.77, and 1.75, respectively. Meanwhile, the magnitude of the gradient is also large. Figure 8(2) shows the field distribution for $d/r = 1.75$. Figure 8(3) shows the gradient distribution along *z-axis* and its MUA for different uniformity deviations of 2%, 1%, and 0.5%.

Therefore, to obtain the best uniform gradient field, the use of a coil pair with currents flowing in opposite directions in each coil and with $d/r = 1.75$ was a perfect choice. In a special case where $d/r = 1.73$, it represents a conventional Maxwell coil pair. The result proved that the conventional Maxwell coil pair is one of the best loop-shaped coil pairs to induce uniform gradient field.

3.4 Implementing the 2-dimensional EMA System

After optimizing the coil parameters, we implemented the 2-dimensional EMA system by combining the two kinds of coils. We chose the superposition of uniform magnetic and gradient fields as the most remarkable characteristic of the field. Thus, we can choose two pairs of orthogonal uniform field coil with parameter $d/r = 1.02$ to induce a uniform field. A single pair of uniform gradient field coils with parameter $d/r = 1.75$ is sufficient to induce uniform gradient field because it can induce gradients in both the radial and axial directions. Figure 9 shows the schematic of the EMA system.

3.5 Discussion of the Optimization Method

In this section, we proposed a simple method to design and optimize a coil pair. Initially, this method was

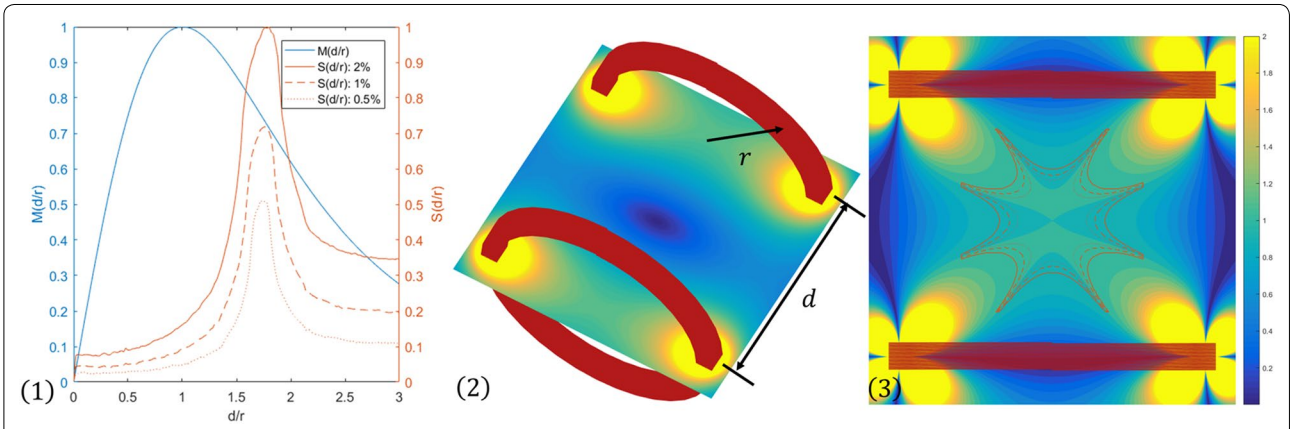

Figure 8 Optimization result for the loop-shaped coil pair inducing uniform gradient field

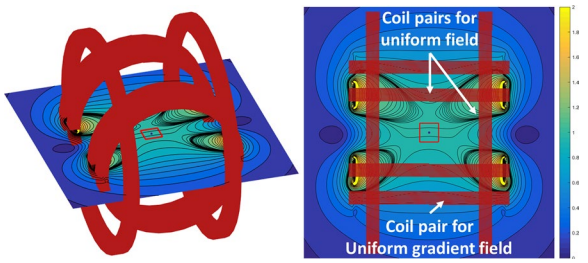

Figure 9 Schematic of the EMA system

implemented by determining characteristics of the magnetic field, which is assumed as a superposition of the uniform magnetic and gradient fields in this case. Then, we chose different shapes of the coil pair and its parameters to be optimized. Subsequently, appropriate optimization operators were chosen to optimize the coil pair. Finally, the EMA system was implemented by combining the optimized coil pair. A large variety of EMA systems [24, 27, 28, 38] were proposed and optimized through this method, although they were not strictly implemented in a step-by-step manner.

This method achieves several advantages in design and optimization of EMA systems composed of X-shaped coil pair, including but not limited to, loop-shaped, oval-shaped, square-shaped, rectangle-shaped, capsule-shaped, and even saddle-shaped coil pairs. Theoretically speaking, the optimization process is applicable for coil pair configurations of any shape, to quantitatively analyze and optimize it, provided the magnetic field distribution expressions and its partial derivative with respect to position can be obtained. Moreover, because the most significant characteristics of the field were determined in Section 3.1, the main difficulties of the process lie in the optimization of the parameters of the coil. Determining the ideal methods for choosing the best parameters of the coil pair and appropriate optimization operators are major concerns.

Derivation of the magnetic field distribution of the X-shaped coil required a great deal of patience, as it was the fundamentals of the subsequent studies, and it was prone to errors. This paper also presents the magnetic field distribution of a single rectangle-shaped coil in Section 2, which can be directly used in the design and optimization process.

However, this method also has its own limitations. It mainly concentrates on coil pairs generating a uniform magnetic or gradient field or the superposition of these fields. Therefore, this method mainly focuses on the design and optimization of a gradient-based-field EMA system. It was not appropriate to apply this to the other two kinds of driving fields, i.e., alternating and rotating field, because of the essential change in the driving mechanism.

3.6 Applicability of the Optimization Method

As discussed in Section 3.5, the newly proposed design and optimization method is applicable to coil pairs in any shape. Here, we briefly present the optimization results of applying it to the squared-shaped and rectangle-shaped coil pairs. The EMA system composed of other shapes of coil pair configurations could be optimized through the same process discussed in Sections 3.1–3.4.

For a square-shaped coil pair, the parameter to be optimized was d/w, where w is width of the square coil, d is distance between the two coils.

The optimization result of the squared-shaped coil pair inducing uniform magnetic field was shown in Figure 10. Figure 10(1) shows $M(d/w)$ and $S(d/w)$ of the field. For different uniformity deviations of 2%, 1%, and 0.5%, $S(d/w)$ reaches the maximum when $d/w = 0.590, 0.570,$

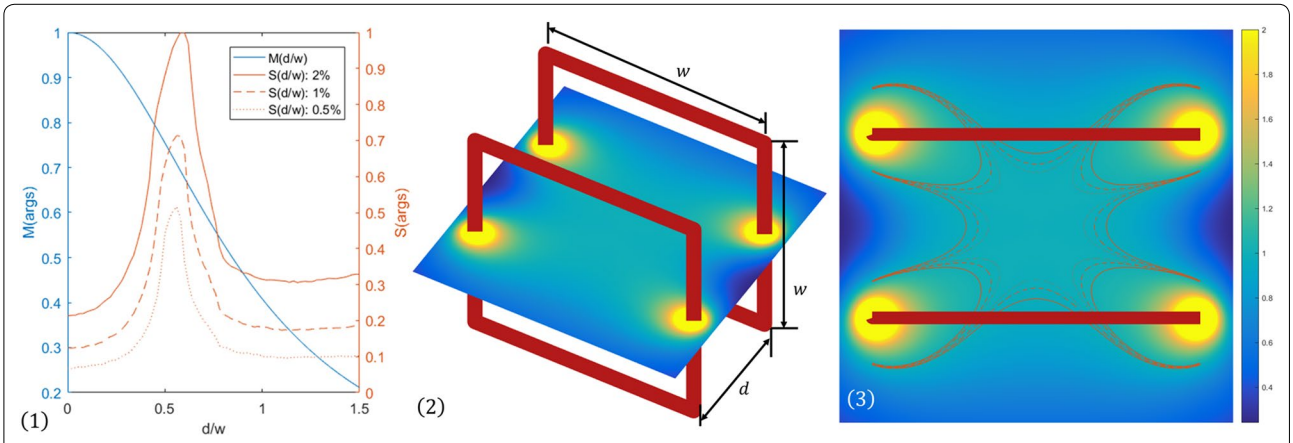

Figure 10 Optimization result for the squared-shaped coil pair inducing uniform magnetic field

and 0.558, respectively. Meanwhile, the magnitude of the field is also large. Figure 10(2) shows the distribution of the field for $d/w = 0.558$. Figure 10(3) shows the MUA of the uniform field for different uniformity deviations of 2%, 1%, and 0.5%.

The optimization result of the squared-shaped coil pair inducing uniform gradient field was shown in Figure 11. Figure 11(1) shows $M(d/w)$ and $S(d/w)$ of the field. For different uniformity deviations of 2%, 1%, and 0.5%, $S(d/w)$ reaches the maximum when $d/w = 0.982$, 0.966, and 0.958, respectively. Meanwhile, the magnitude of gradient of the field is also large. Figure 11(2) shows the distribution of the field for $d/w = 0.958$. Figure 11(3) shows the gradient distribution along z-axis the MUA of the uniform gradient for different uniformity deviations of 2%, 1%, and 0.5%.

For a rectangle-shaped coil pair, the parameters to be optimized were h/w and d/w, where w and h are the width and height of the rectangle coil, respectively, d is distance between the two coils.

The optimization result for the rectangle-shaped coil pair inducing uniform magnetic field is shown in Figure 12. The best parameters are $h/w = [0.9, 1.1]$, $d/w = [0.5, 0.6]$, of which the best values are $h/w = 1.015$, $d/w = 0.56$.

The optimization result for the rectangle-shaped coil pair inducing uniform gradient field is shown in Figure 13. The best parameters are $h/w = [1.0, 1.2]$, $d/w = [0.9, 1.1]$, of which the best values are $h/w = 1.10$, $d/w = 1.00$.

Other coil configurations were basically a combination of loop/arc coil and line coil. The optimization process was the same as the loop- and rectangle-shaped coil pairs.

4 Simulation Results of Motion Control

Numerical simulations of target trajectory tracking were performed to test the controllability of the coils designed in Section 3. Thus, we verified the validity of the models and coil pair configuration design and optimization method. The trajectory tracking procedure is described as

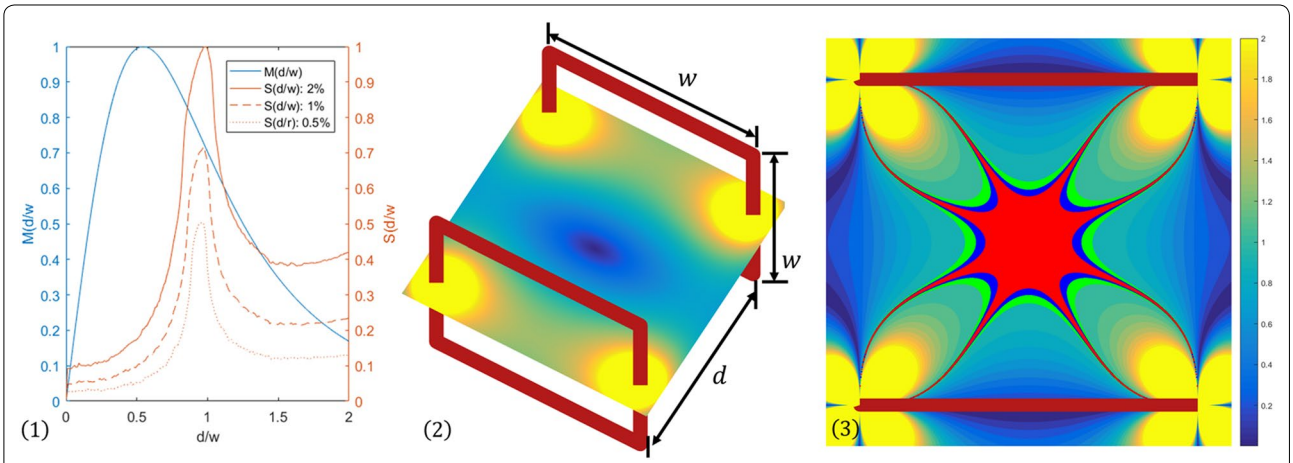

Figure 11 Optimization result for the squared-shaped coil pair inducing uniform gradient field

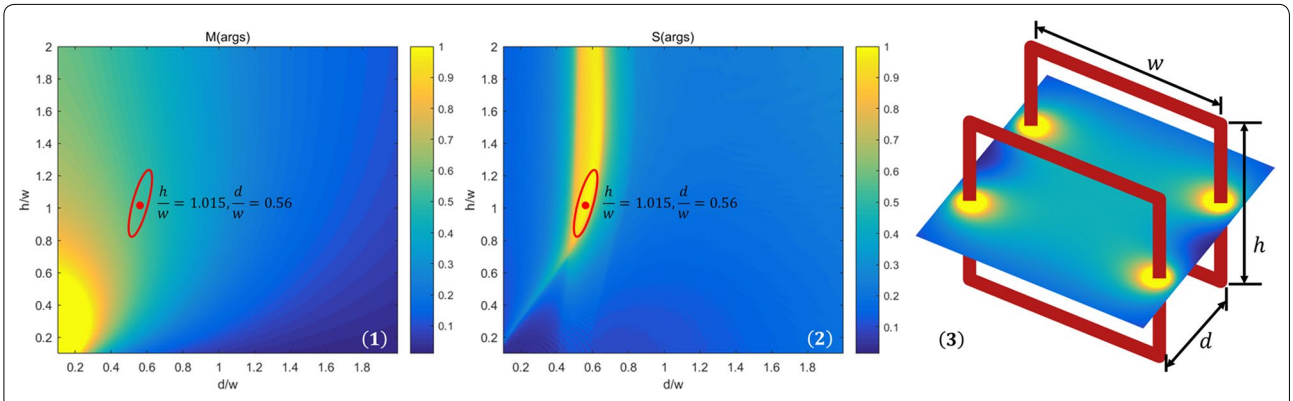

Figure 12 Optimization result for the rectangle-shaped coil pair inducing uniform magnetic field

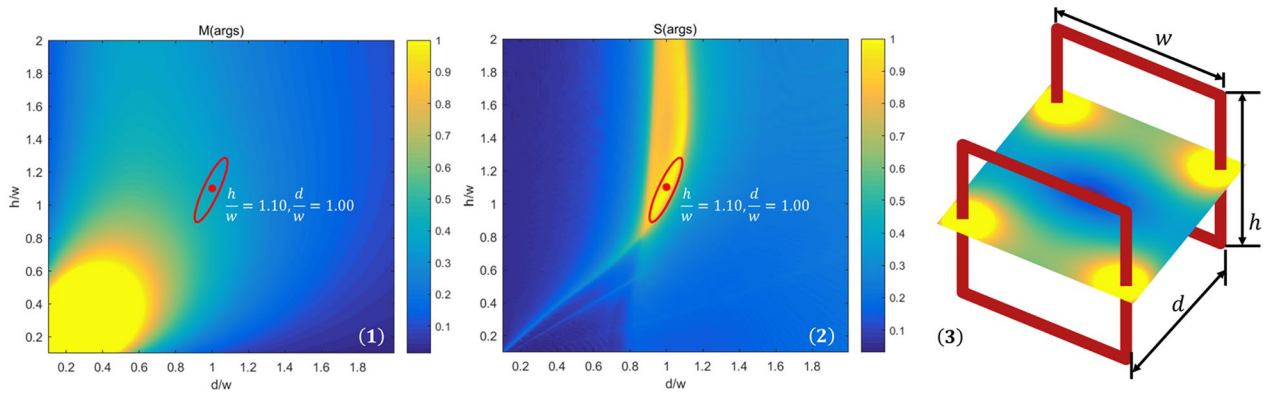

Figure 13 Optimization result for the rectangle-shaped coil pair inducing uniform gradient field

follows: Initially, a desired 2-dimensional (2-D) targeted trajectory $\boldsymbol{X}_0$ of the microparticle was specified. Secondly, the position of the microparticles were detected by the position measure technique, and the velocity of the particle was determined using the traditional position differentiation method. Thirdly, proper currents flowing in the Helmholtz coils were calculated through feedback control algorithms and the currents flowing in the Maxwell coils were maintained constant. Finally, magnetic forces were generated by the current-carrying coils to drive the microparticle. Thus, the microparticle was controlled automatically to track the targeted trajectory.

Trajectory tracking of the microparticle was implemented through the control flow chart shown in Figure 14. The control feedback block is an input-to-state stability controller [25], which computes the currents to be applied to the coils, by the following equation:

$$\begin{aligned} I_{helm} =& mk_0\left(1 + k_1k_2 + \frac{k_2}{2\delta^2}\right)\boldsymbol{E}_1 + mk_0\left(\ddot{\boldsymbol{X}}_0 + \frac{\mu}{m}\dot{\boldsymbol{X}}_0\right) \\ &+ mk_0\left(-\frac{\mu}{m} + k_1 + k_2 + \frac{1}{2\delta^2}\right)\boldsymbol{E}_2, \end{aligned} \tag{45}$$

where k_0, k_1, k_2, and δ are parameters of the controller. μ is the damping coefficient of the medium. m is mass of the microparticle. $\boldsymbol{E}_1$ and $\boldsymbol{E}_2$ are position and velocity tracking errors, respectively, which are calculated based on targeted trajectory and the measured trajectory provided by the position measurement block, given by:

$$\begin{aligned} \boldsymbol{E}_1 &= \tilde{\boldsymbol{X}} - \boldsymbol{X}_0, \\ \boldsymbol{E}_2 &= \dot{\tilde{\boldsymbol{X}}} - \dot{\boldsymbol{X}}_0, \end{aligned} \tag{46}$$

where $\boldsymbol{X}_0, \dot{\boldsymbol{X}}_0$ are the desired position and velocity, respectively. $\tilde{\boldsymbol{X}}, \dot{\tilde{\boldsymbol{X}}}$ are the measured position and velocity, respectively. The control feedback block computes currents flowing in the two orthogonal Helmholtz coils and allows the system to pull a microparticle towards the targeted position.

Further, measurement errors and environmental noises were both taken into consideration to simulate the real environment. Therefore, the measured trajectory and dynamic force were expressed as:

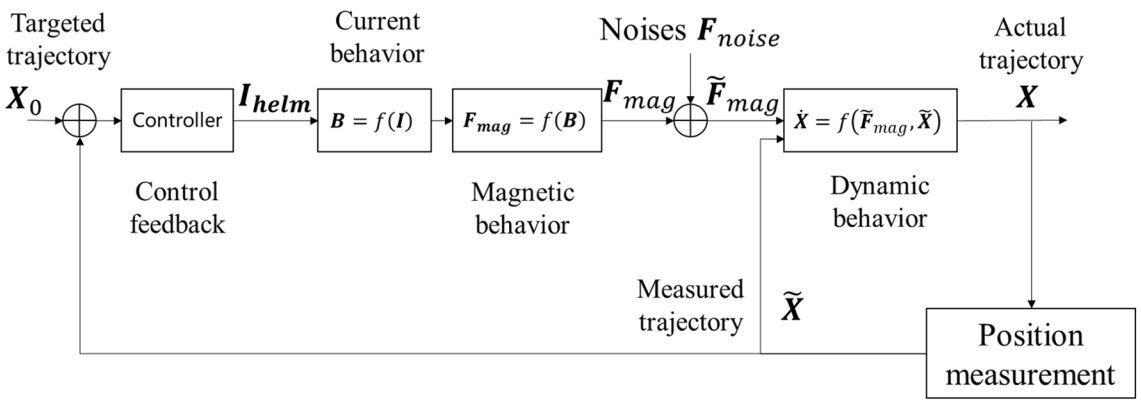

Figure 14 Schematic of the closed loop motion control

$$\tilde{\boldsymbol{X}} = \boldsymbol{X} + \boldsymbol{N},$$
$$\tilde{\boldsymbol{F}}_{mag} = \boldsymbol{F}_{mag} + \boldsymbol{F}_{noise}, \tag{47}$$

where $\boldsymbol{N}$ denotes the measurement errors generated by the random function in MATLAB, with an amplitude of $[-0.01, 0.01]^*\boldsymbol{X}$. $\boldsymbol{F}_{noise}$ denotes the environmental noises generated by MATLAB random function, with an amplitude of $[-0.1, 0.1]^*\boldsymbol{F}_{mag}$.

The microparticle was manipulated to track an in-plane 2-D spiral curve expressed as

$$x_0 = 0.75(t+2)\cos\left(\frac{\pi}{5}\right) \text{ mm},$$
$$y_0 = 0.75(t+2)\sin\left(\frac{\pi}{5}+\frac{\pi}{6}\right) \text{ mm}. \tag{48}$$

Figure 15 shows the simulation results for controller parameter of $k_0 = 10^5$, $k_1 = k_2 = 40$, $\delta = 0.5$. Figure 15(1)–15(3) show the target trajectory (in blue) of the particle and the tracking trajectory (in red) at various time instants, t = 1.0 s, 7.0 s, 12.0 s, respectively. Figure 15(4) shows the position tracking errors $\boldsymbol{E}_1$. Figure 15(5) shows the velocity tracking errors $\boldsymbol{E}_2$. Figure 15(6) shows the feedback current $\boldsymbol{I}_{helm}$. The simulation results demonstrated good controllability of the EMA system.

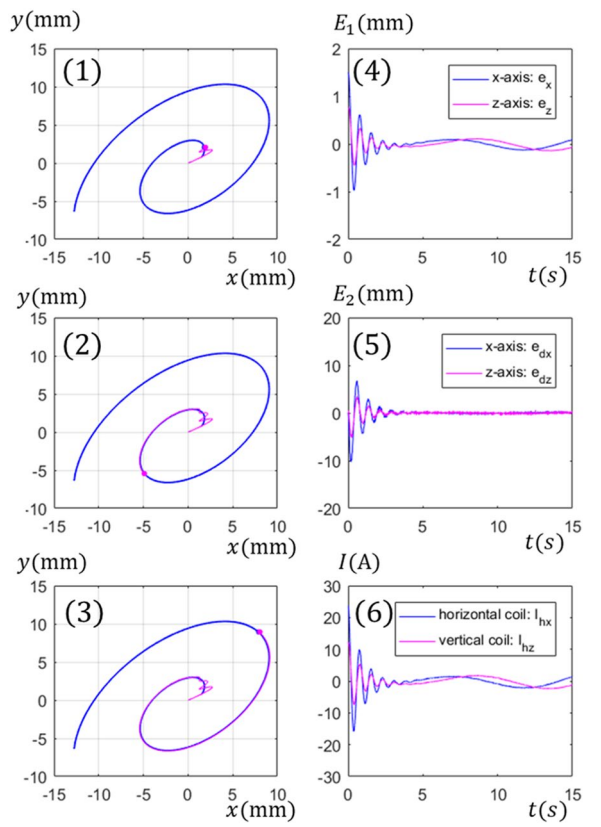

Figure 15 Simulation results

5 Conclusions

(1) This paper proposed the modeling of an EMA system, including the three processes: 1) Different shapes of single current-carrying coil induced magnetic field; 2) The externally applied field exerted magnetic forces and torques on a ferromagnetic object; 3) The exerted forces and torques drove the ferromagnetic object to move. The three models fully described the behaviors of a ferromagnetic object controlled by the EMA system.

(2) A simple and efficient method for coil configuration design and optimization was proposed, which mainly focused on gradient-field-based driving EMA system. The method included four steps: determining the most critical characteristics of the magnetic field according to the specific requirements; choosing appropriate types of coil, including shapes of the coil and coil parameters to be optimized; optimizing the coil configuration by choosing appropriate optimization operators as listed in Section 3.3.1; and finally, implementing the EMA system using the optimized coil pair.

(3) A loop-shaped coil pair was chosen to demonstrate the method clearly and practically. The optimization result demonstrated that the best distance to radius ratio of a loop-shaped coil pair was 1.02 for uniform magnetic field and 1.75 for uniform gradient field, respectively. We observed that these are the values demonstrated by the conventional Helmholtz and Maxwell coil pairs. The newly proposed method is applicable to any-shaped coil pair. Applicability of the method on other coil configurations, such as square-shaped and rectangle-shaped coil pair, was discussed, the results of which were demonstrated.

(4) Simulations of a microparticle tracking the target trajectory were conducted to show the performance of the coil pair designed by the newly proposed method. The results demonstrated good controllability.

Authors' Contributions

XJ took on most of the research work, including the theoretical research and modeling, proposal and establishment of the new method and simulation work, and paper writing of the manuscript. WG put forward a great variety of valuable suggestions on some key theory points, assisted with the theory researching and method validity, so that the research work can be carried out smoothly. All authors read and approved the final manuscript.

Authors' Information

Xiaolong Jing, born in 1993, is currently a master candidate at *Institute of Design and Control Engineering for Heavy Equipment, School of Mechanical Engineering, Shanghai Jiao Tong University, China*. He received his bachelor's degree from *Shanghai Jiao Tong University, China*, in 2017. His research interests include robotics, magnetically controlled micro-robot and machine vision.

Weizhong Guo, is currently a professor at *School of Mechanical Engineering, Shanghai Jiao Tong University, China*. He received his PhD degree from *Shanghai Jiao Tong University, China*, in 1999. He was an Assistant Professor at SJTU (1999-2001) and Associate Professor at SJTU (2001-2009) and became a Full Professor at SJTU in 2009. His research mainly focuses on parallel robots and modern mechanisms.

Competing Interests

The authors declare that they have no competing interests.

Funding

Supported by Aerospace Research Project (Grant No. 040102).

Received: 11 May 2018 Revised: 18 January 2019 Accepted: 11 July 2019
Published online: 23 July 2019

References

[1] T E Mallouk, A Sen. Powering nanorobots. *Scientific American*, 2009, 300(5): 72-77.
[2] J Wang, W Gao. Nano/microscale motors: Biomedical opportunities and challenges. *ACS Nano*, 2012, 6(7): 5745-5751.
[3] B J Nelson, I K Kaliakatsos, J J Abbott. Microrobots for minimally invasive medicine. *Annual Review of Biomedical Engineering*, 2010, 12: 55-85.
[4] J J Abbott, K E Peyer, M C Lagomarsino, et al. How should microrobots swim? *The International Journal of Robotics Research*, 2009, 28(11-12): 1434-1447.
[5] G Chatzipirpiridis, E Avilla, O Ergeneman, et al. Electroforming of magnetic microtubes for microrobotic applications. *IEEE Transactions on Magnetics*, 2014, 50(11): 1-3.
[6] X Chen, M Hoop, F Mushtaq, et al. Recent developments in magnetically driven micro- and nanorobots. *Applied Materials Today*, 2017, 9: 37-48.
[7] L Zhang, H Huang, L Chen, et al. A magnetically controlled micro-robot with multiple side flagella. *IEEE International Conference on Nano/Micro Engineered and Molecular Systems (NEMS)*, 2017: 544-549.
[8] I S M Khalil, H C Dijkslag, L Abelmann, et al. MagnetoSperm: A microrobot that navigates using weak magnetic fields. *Applied Physics Letters*, 2014, 104(22): 223701.
[9] D Byun, J Choi, K Cha, et al. Swimming microrobot actuated by two pairs of Helmholtz coils system. *Mechatronics*, 2011, 21(1): 357-364.
[10] S Floyd, C Pawashe, M Sitti. An untethered magnetically actuated micro-robot capable of motion on arbitrary surfaces. *IEEE International Conference on Robotics and Automation (ICRA)*, 2008: 419-424.
[11] C Pawashe, S Floyd, M Sitti. Modeling and experimental characterization of an untethered magnetic micro-robot. *International Journal of Robotics Research*, 2009, 28(8): 1077-1094.
[12] P J Vach, D Fairve. The triathlon of magnetic actuation: Rolling, propelling, swimming with a single magnetic material. *Scientific Reports*, 2015, 5(1): https://doi.org/10.1038/srep09364.
[13] L Zhang, J J Abbott, L Dong, et al. Artificial bacterial flagella: Fabrication and magnetic control. *Applied Physics Letters*, 2009, 94(6): 64107.
[14] Z L Hang, K E Peyer, B J Nelson. Artificial bacterial flagella for micromanipulation. *Lab on a Chip*, 2010, 10(17): 2203-2215.
[15] S Tottori, L Zhang, F Qiu, et al. Magnetic helical micromachines: fabrication, controlled swimming, and cargo transport. *Advanced Materials*, 2012, 24(6): 811-816.
[16] A W Mahoney, N D Nelson, K E Peyer, et al. Behavior of rotating magnetic microrobots above the step-out frequency with application to control of multi-microrobot systems. *Applied Physics Letters*, 2014, 104(14): 144101.
[17] I S Khalil, J D Keuning, L Abelmann, et al. Wireless magnetic-based control of paramagnetic microparticles. *IEEE Ras & Embs International Conference on Biomedical Robotics & Biomechatronics*, 2012.
[18] I Khalil, P Ferreira, R Eleutério, et al. Magnetic-based closed-loop control of paramagnetic microparticles using ultrasound feedback. *IEEE International Conference on Robotics and Automation (ICRA)*, 2014: 3807-3812.
[19] E Diller, J Giltinan, G Z Lum, et al. Six-degree-of-freedom magnetic actuation for wireless microrobotics. *The International Journal of Robotics Research*, 2016, 35(1-3): 114-128.
[20] M Dkhil, M Kharboutly, A Bolopion, et al. Closed-loop control of a magnetic particle at the air–liquid interface. *IEEE Transactions on Automation Science and Engineering*, 2017, 14(3): https://doi.org/10.1109/tase.2015.2448133.
[21] A Bolopion, S Bouchebout, S Régnier. Fast, repeatable and precise magnetic actuation in ambient environments at the micrometer scale. *Journal of Micro-Bio Robotics*, 2017, 13(1-4): 55-66.
[22] S Bouchebout, A Bolopion, M Gautier, et al. Position control of a ferromagnetic micro-particle in a dry environment. *IEEE International Conference on Advanced Intelligent Mechatronics (AIM)*, 2014: 1-6.
[23] F Niu, W Ma, H K Chu, et al. An electromagnetic system for magnetic microbead's manipulation. *IEEE International Conference on Mechatronics and Automation*, 2015: 1005-1010.
[24] F Niu, J Li, W Ma, et al. Development of an enhanced electromagnetic actuation system with enlarged workspace. *Transactions on Mechatronics*, 2017, 22(5): 2265-2276.
[25] W Ma, J Li, F Niu, et al. Robust control to manipulate a microparticle with electromagnetic coil system. *Transactions on Industrial Electronics*, 2017, 64(11): 8566-8577.
[26] K B Yesin, K Vollmers, B J Nelson. Modeling and control of untethered biomicrorobots in a fluidic environment using electromagnetic fields. *International Journal of Robotics Research*, 2006, 25(5-6): 527-536.
[27] X Zhang, C Duan, L Liu, et al. Novel electromagnetic actuation (EMA) method for 3-dimensional locomotion of intravascular microrobot. *Sensors and Actuators A-Physical*, 2010, 157(1): 118-125.
[28] S Jeon, G Jang, H Choi, et al. Magnetic navigation system with gradient and uniform saddle coils for the wireless manipulation of micro-robots in human blood vessels. *IEEE Transactions on Magnetics*, 2010, 46(6): 1943-1946.
[29] G Go, H Choi, S Jeong, et al. Electromagnetic navigation system using simple coil structure (4 coils) for 3-D locomotive microrobot. *IEEE Transactions on Magnetics*, 2015, 51(4): 1-7.
[30] M P Kummer, J J Abbott, B E Kratochvil, et al. OctoMag: An electromagnetic system for 5-DOF wireless micromanipulation. *IEEE Transactions on Robotics*, 2010, 26(6): 1006-1017.
[31] J Yu, T Xu, Z Lu, et al. On-demand disassembly of paramagnetic nanoparticle chains for microrobotic cargo delivery. *IEEE Transactions on Robotics*, 2017, 33(5): 1213-1225.
[32] N Derby, S Olbert. Cylindrical magnets and ideal solenoids. *American Journal of Physics*, 2010, 78(3): 229-235.
[33] V Labinac, N Erceg, D Kotnikkaruza. Magnetic field of a cylindrical coil. *American Journal of Physics*, 2006, 74(7): 621-627.
[34] P F Byrd, M D Friedman. *Handbook of elliptic integrals for engineers and physicists*. Springer, 2013.
[35] J J Abbott, O Ergeneman, M P Kummer, et al. Modeling magnetic torque and force for controlled manipulation of soft-magnetic bodies. *IEEE Transactions on Robotics*, 2007, 23(6): 1247-1252.
[36] J A Osborn. Demagnetizing factors of the general ellipsoid. *Physical Review*, 1945, 67(11-12): 351.
[37] M Beleggia, M Degraef, Y T Millev. The equivalent ellipsoid of a magnetized body. *Journal of Physics D: Applied Physics*, 2006, 39(5): 891.
[38] J Choi, H Choi, K Cha, et al. Two-dimensional locomotive permanent magnet using electromagnetic actuation system with two pairs stationary coils. *IEEE International Conference on Robotics and Biomimetics (ROBIO)*, 2009: 1166-1171.
[39] H H Yong, B H Han, S Y Lee. Magnetic propulsion of a magnetic device using three square-Helmholtz coils and a square-Maxwell coil. *Medical & Biological Engineering & Computing*, 2010, 48(2): 139-145.